



Single-atom Pt–N₄ active sites anchored on porous C₃N₄ nanosheet for boosting the photocatalytic CO₂ reduction with nearly 100% CO selectivity

Shan Hu^a, Panzhe Qiao^{c,*}, Xinming Liang^a, Guiming Ba^a, Xiaolong Zu^d, Huilin Hu^a, Jinhua Ye^{a,b,**}, Defa Wang^{a,*}

^a TJU-NIMS International Collaboration Laboratory, Key Laboratory of Advanced Ceramics and Machining Technology (Ministry of Education) and Tianjin Key Laboratory of Composite and Functional Materials, School of Materials Science and Engineering, Tianjin University, Tianjin 300072, China

^b International Center for Materials Nanoarchitectonics (WPI-MANA), National Institute for Materials Science (NIMS), Tsukuba 305-0044, Ibaraki, Japan

^c Shanghai Synchrotron Radiation Facility, Shanghai Advanced Research Institute, Chinese Academy of Sciences, Shanghai 201210, China

^d Hefei National Research Center for Physical Science at Microscale, National Synchrotron Radiation Laboratory, University of Science and Technology of China, Hefei 230026, China

ARTICLE INFO

Keywords:

Pt single atom
C₃N₄
Pt–N₄ coordination
CO₂ photoreduction
CO selectivity

ABSTRACT

Photoreduction of CO₂ and H₂O into fuels and value-added chemicals is a promising green technology for solar-to-chemical conversion. However, improving the conversion efficiency with regulated product selectivity is a big challenge due to the sluggish dynamic transfer and insufficient active sites. Herein, we report on Pt single atoms anchored porous C₃N₄ nanosheet photocatalyst (Pt₁@CN) with Pt–N₄ coordination for stable and efficient CO₂ photoreduction using H₂O as reductant. The Pt₁@CN exhibits an evolution rate of 84.8 μmol g^{−1} h^{−1} with nearly 100% CO selectivity, outperforming most previous C₃N₄-based single-atom photocatalysts. Experimental and DFT calculation results reveal that the Pt–N₄ coordinated active sites promote the photogenerated electron transfer, CO₂ adsorption/activation, *COOH generation, and *CO desorption, thus accounting for the significantly improved CO₂ photoreduction activity with ~100% CO selectivity. This study provides a deep insight into the significant roles of single-atom active sites in enhancing the CO₂ photoreduction activity and regulating the product selectivity.

1. Introduction

Solar-driven conversion of carbon dioxide (CO₂) and water (H₂O) into high-value-added chemicals is a promising strategy to mitigate excessive carbon emissions and achieve low-carbon and sustainable development [1,2]. However, this process usually suffers from several drawbacks including complicated multiple reaction pathways, sluggish kinetics, insufficient active sites, and the possible competing hydrogen evolution reaction (HER), which limit its practical application [3–5]. Among the various CO₂ reduction products, CO is the most common and a vital feedstock for chemical and industrial applications such as Fischer–Tropsch synthesis, etc [6–8]. Over the past two decades, noble metal based catalysts have been proven to be highly active for the CO₂-to-CO conversion; however, the high cost and scarcity hinder their

practical large-scale applications [9–11]. Recently, single-atom catalysts (SACs) have attracted considerable interest in CO₂ photoreduction, owing to their maximized atom-utilization efficiency, tunable electronic property, and low-coordinated geometric structure [12–14]. Generally, monodispersed metal atoms can be anchored on a suitable support by introducing defects, replacing in-plane atoms, or coordinating with in-plane atoms [15,16].

Conjugated polymer carbon nitride (C₃N₄) has emerged as an attractive metal-free, visible-light-responsive photocatalyst for CO₂ reduction owing to its facile synthesis, appealing electronic band structure, and high physicochemical stability [17–19]. However, C₃N₄ often suffered a sluggish dynamics of photogenerated charge carriers due to its inherent π-conjugated structure [20,21]. In recent years, loading isolated metal atoms on C₃N₄ support with metal–nitrogen

* Corresponding authors.

** Corresponding author at: TJU-NIMS International Collaboration Laboratory, Key Laboratory of Advanced Ceramics and Machining Technology (Ministry of Education) and Tianjin Key Laboratory of Composite and Functional Materials, School of Materials Science and Engineering, Tianjin University, Tianjin 300072, China.

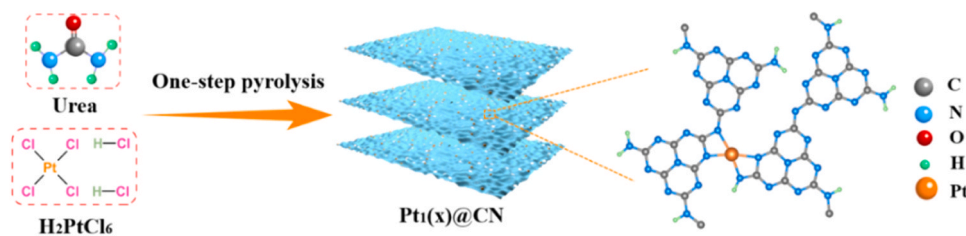
E-mail addresses: qiaopz@sari.ac.cn (P. Qiao), jinhua.ye@nims.go.jp (J. Ye), defawang@tju.edu.cn (D. Wang).

<https://doi.org/10.1016/j.apcatb.2024.123737>

Received 3 November 2023; Received in revised form 22 December 2023; Accepted 13 January 2024

Available online 15 January 2024

0926-3373/© 2024 Elsevier B.V. All rights reserved.



Scheme 1. Schematic illustration of synthetic process of the $\text{Pt}_1(\text{x})@\text{CN}$ photocatalysts.

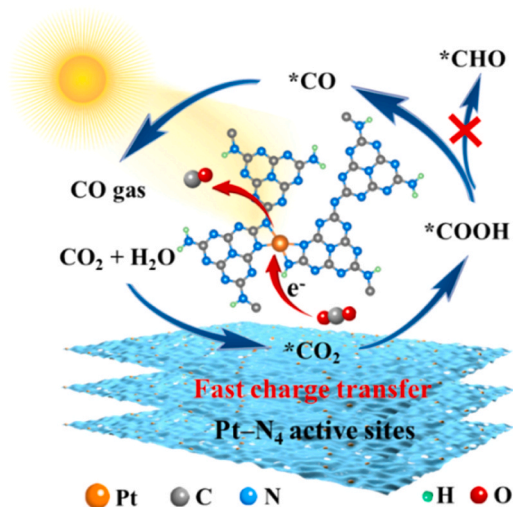
(M–N) coordination has been attracting increasing attention in the development of highly efficient SACs, since the C_3N_4 framework with electron-rich N atoms can provide sufficient coordination sites and favorable space for embracing metal single atoms through the formation of M–N bonds [22,23]. Xiao *et al.* synthesized Fe single atoms decorated C_3N_4 with Fe– N_4 coordination environment for selective oxidation of ethylbenzene [24]. Zhang *et al.* revealed the mechanism for the significantly enhanced H_2 evolution efficiency by direct observation of the dynamic bond evolution in the as-synthesized single-atom Pt/ C_3N_4 photocatalyst [25]. Hu *et al.* reported a Pt SAs/ C_3N_4 photocatalyst with the Pt– N_3 bond showing enhanced performance of photocatalytic H_2 evolution due to the promoted charge separation and transfer [26]. Chen *et al.* synthesized rare-earth La single atoms on C_3N_4 with dispersed La–N sites for efficient photocatalytic CO_2 reduction [27]. Our recent study demonstrated that the strong metal–support interaction (Ag– N_3 coordination) could effectively accelerate the dynamic transfer of photoexcited charge carriers between C_3N_4 and Ag single atoms, and hence significantly enhance the activity and CO selectivity (94%) for CO_2 photoreduction [28]. The previous results demonstrated that the introduction of metal single atoms [29–32] or decreasing the size of metal nanoparticles [33–35] could enhance the photoreduction efficiency by accelerating the charge transfer dynamics due to the shortened electron transfer distance. However, it is still a big challenge to achieve high efficiency and 100% selectivity of a single product in CO_2 photoreduction because of the difficulty in modulation of reaction kinetics involving multiple protons/electrons, and the lack of immediate desorption of intermediates and final product.

Herein, we developed a facile one-step pyrolysis process to fabricate a series of Pt single atoms anchored porous C_3N_4 nanosheets ($\text{Pt}_1(\text{x})@\text{CN}$, where x is the content of Pt in wt%) for CO_2 photoreduction. The optimal $\text{Pt}_1(0.519)@\text{CN}$ photocatalyst (hereinafter referred to as $\text{Pt}_1@\text{CN}$) exhibited considerably enhanced CO_2 photoreduction activity (CO evolution rate: $84.8 \mu\text{mol g}^{-1} \text{h}^{-1}$) with nearly 100% CO selectivity using H_2O as a reductant, which surpassed most of the previous work on C_3N_4 -based single atom photocatalysts in terms of both the CO evolution rate and selectivity. The Pt atomic dispersion and specific Pt– N_4 coordination were confirmed via aberration-corrected high-angle annular dark-field scanning transmission electron microscopy (AC-HAADF-STEM) and X-ray absorption fine structure (XAFS) spectroscopy. Experimental and density functional theory (DFT) calculation results indicated that the Pt– N_4 coordinated single atoms served as active sites to promote the dynamic transfer of photogenerated charge carriers, adsorption and activation of CO_2 molecules for generating $^*\text{COOH}$, and rapid desorption of $^*\text{CO}$, thereby enhancing the photocatalytic CO_2 reduction activity with nearly 100% CO selectivity. This study suggests a feasible strategy of constructing single-atom active sites in a suitable support for enhancing the CO_2 photoreduction efficiency and modulating the product selectivity.

2. Experimental section

2.1. Chemicals and materials synthesis

Urea ($\text{CH}_4\text{N}_2\text{O}$) and chloroplatinic acid (H_2PtCl_6) were obtained



Scheme 2. The Pt– N_4 coordinated single atoms anchored on C_3N_4 nanosheet accelerate the transfer of photogenerated electrons for boosting the CO_2 photoreduction activity and CO selectivity.

from Aladdin Reagent Corporation. All reagents were used as required without purification steps. As shown in Scheme 1, Pt single atoms anchored porous C_3N_4 nanosheets photocatalysts ($\text{Pt}_1(\text{x})@\text{CN}$, x is the content of Pt in wt%) were synthesized via a facile one-step pyrolysis process. Typically, 40 g urea was mixed thoroughly with different amounts (1, 3, 5 mL) of H_2PtCl_6 aqueous solution (0.01 g mL^{-1}) at room temperature, then the resulting precipitates were transferred into a muffle furnace and annealed in an air atmosphere at 500°C for 2 h with a ramping rate of 3°C min^{-1} , obtaining a series of photocatalysts $\text{Pt}_1(\text{x})@\text{CN}$. The actual Pt contents in the as-synthesized $\text{Pt}_1(\text{x})@\text{CN}$ photocatalysts were measured to be 0.137, 0.519, and 0.919 wt%, respectively, using inductively coupled plasma–optical emission spectroscopy (ICP–OES). For simplicity, the optimal $\text{Pt}_1(0.519)@\text{CN}$ photocatalyst was denoted as $\text{Pt}_1@\text{CN}$. For comparison, porous C_3N_4 nanosheet sample was prepared following the procedure for the synthesis of $\text{Pt}_1(\text{x})@\text{CN}$ without adding H_2PtCl_6 .

2.2. Characterizations

Transmission electron microscopy (TEM) images, High-resolution TEM images (HRTEM, JEOL JEM-2100plus, Japan) and aberration-corrected high-angle annular dark-field scanning TEM images (AC-HAADF-STEM, TALOS F200X microscope) were adopted to observe the morphologies and structures of the samples. Inductively coupled plasma–optical emission spectroscopy (ICP–OES) was performed on an America Agilent (Agilent ICP–OES720). Brunauer–Emmett–Teller (BET) surface area, pore size and porosity were measured by using N_2 adsorption/desorption on a BELSORP-II mini (MicrotracBEL, Japan) nitrogen adsorption apparatus. The X-ray diffraction (XRD) measurements were carried out on an X-ray diffractometer (Cu– $\text{K}\alpha$ radiation source, D8 Advanced, Bruker, Germany). X-ray photoelectron

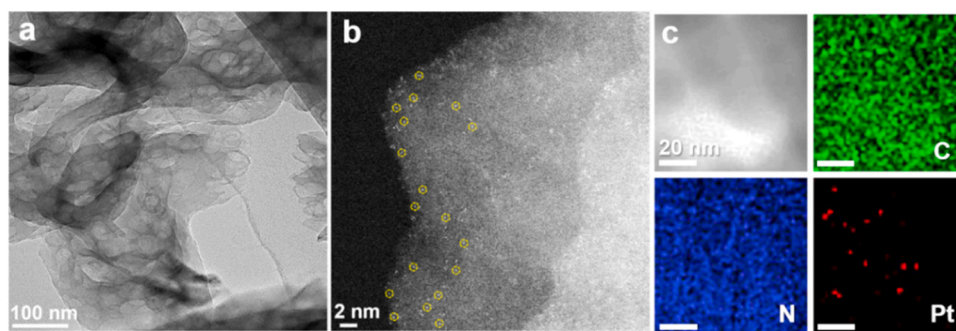


Fig. 1. (a) HRTEM image, (b) AC-HAADF-STEM image, and (c) elemental mapping images of Pt₁@CN.

spectroscopy (XPS) studies were performed using Al K α radiation as the excitation source (Thermo Fisher ESCALAB 250Xi). All the binding energies were calibrated by the C 1 s spectrum at 284.8 eV. UV–vis absorption spectra were determined at room temperature on a spectrophotometer (UV-2700, Shimadzu, Japan). Fourier transform infrared (FTIR) spectroscopy and in situ diffuse reflectance infrared Fourier transform (DRIFT, see details in [Supplementary data](#)) spectroscopy were performed on a Nicolet 6700 Fourier transform instrument. Photoluminescence (PL) measurement was conducted on a fluorescence spectrometer (Fluorolog-3, Horiba Scientific, USA) at an excitation wavelength of 375 nm. The Pt L₃-edge X-ray absorption fine structure spectroscopy (XAFS) was measured at the Shanghai Synchrotron Radiation Facility (SSRF, China. See details in [Supplementary data](#)). Synchrotron-radiation vacuum ultraviolet photoionization mass spectrometry (SVUV-PIMS) was carried out at the combustion endstation of the BL04B beamline at the National Synchrotron Radiation Laboratory (NSRL, Hefei, China). The CO₂ temperature-programmed desorption (CO₂-TPD) and CO temperature-programmed desorption (CO-TPD) were performed on a multifunction chemisorption analyzer (PX 200A, Pengxiang Technology, China) with a quartz U-tube reactor and was monitored by a thermal conductivity detector. To eliminate contaminations, the sample was pretreated at 200 °C for 1 h in an Ar atmosphere before analysis. After the temperature was decreased to 40 °C, the sample was swept with CO₂ for 30 min and then with Ar to remove the physisorbed CO₂ molecules until the baseline was flat. Then, the temperature was heated to 500 °C (heating rate: 10 °C min⁻¹) to obtain the CO₂-TPD curve.

2.3. Evaluation of photocatalytic CO₂ reduction

Evaluation of CO₂ photoreduction was carried out in a closed-circulated reaction system (OLPCRS-3, Shanghai Boyi Scientific Instrument Co., China). 10 mg as-prepared sample was uniformly spread onto a porous shape air-permeable quartz fiber filter, which was fixed on the stage at the center of the reactor bottom. 3 mL of deionized water was injected into the reaction cell as the reductant, and the photocatalyst was not in direct contact with H₂O. After evacuating the reaction system, 330 mL high-purity CO₂ (99.999%) was introduced and the pressure was kept at ~70 kPa. The photocatalytic CO₂ reduction was initiated under irradiation from a 300 W Xe lamp combined with a standard AM 1.5 G filter (CEL-HXF300, CEAU-light Co., Ltd., Beijing, China; light intensity: ~100 mW cm⁻²; the light spectrum was shown in [Fig. S1](#)). The gaseous products were analyzed by gas chromatograph (GC-2014 C, Shimadzu, Japan) equipped with a Paropak Q chromatographic column with two channels using N₂ as the carrier gas (20 mL min⁻¹). One channel was connected to a methanizer through a flame ionization detector (FID) for the analysis of CO and CO₂. The other channel was connected to the FID for the determination of organic-carbon products (CH₄ etc.). The other gas products (H₂ and O₂) were analyzed by a gas chromatograph (GC-2014, Shimadzu, Japan) equipped with a thermal conductive detector (TCD) using Ar carrier gas (20 mL min⁻¹). The

sampling amount of gaseous products for each test was 0.5 mL.

2.4. DFT calculation

The Vienna ab initio Simulation Package (VASP) were performed in all DFT calculations [36,37]. The Perdew-Burke-Ernzerhof (PBE) exchange-correlation functional and projector augmented wave (PAW) pseudopotential were adopted with spin-polarization [38,39]. During the structure optimization, the convergence criterion of total energy was set to 10⁻⁵ eV, and the atoms were relaxed until the force acting on each atom was less than 0.01 eV/Å. Gaussian smearing of 0.05 eV to the orbital occupation is applied. The plane-wave cut-off energy of 500 eV was used in all computations. Brillouin-zone sampling was carried out with 2 × 3 × 1 Monkhorst-Pack grids. Each slab model was separated from its neighbors by 15 Å vacuum layer spacing. DFT-D3 method of Grimme with the zero-damping function was used in van der Waals (vdW) correction [40,41].

The Gibbs free energies of the CO₂ photoreduction reaction were calculated by correcting the DFT energy with zero-point energy and entropy via $\Delta G = \Delta E + \Delta ZPE - T\Delta S$, where E is the DFT total energy, ZPE is the zero-point energy, T is the environmental temperature, and S is the entropy. For zero-point energy correction and entropy calculations, the vibrational frequencies were calculated by employing density functional perturbation theory. Considering the effect of solvation, we corrected the adsorption energy by using VASPsol [42,43].

3. Results and discussion

The crystal structures of the as-synthesized photocatalysts were examined via X-ray diffraction (XRD). As shown in [Fig. S2](#), the Pt₁(x)@CN (x = 0.137, 0.519, and 0.919 wt%) and CN displayed two typical diffraction peaks of (100) and (002) planes at 13.2° and 27.4°, which could be attributed to the in-plane heptazine motifs and the interlayer stacking of aromatic segments in C₃N₄, respectively [44]. In comparison with CN, the broadening of the characteristic diffraction peaks of (100) and (002) in Pt₁(x)@CN suggested the distortion of the stacking arrangement of the C₃N₄ layers due to the introduction of Pt single atoms [45]. Similarly, the Fourier transform infrared (FTIR) spectra ([Fig. S3](#)) of Pt₁(x)@CN and CN were identical, indicating that the introduction of Pt single atoms did not affect the structure of the C₃N₄ support [46].

We need to mention that in our work, the agglomeration of Pt species was effectively avoided by the release of NH₃ gas during the pyrolysis process of urea. Meanwhile, hierarchical porous structure of Pt₁@CN was formed with the released gas, as evidenced by high-resolution transmission electron microscopic (HRTEM) observation ([Fig. 1a](#)) and nitrogen adsorption–desorption study ([Fig. S4](#)). We need to notify that intrinsically, the BET surface area of Pt₁(x)@CN with broadened characteristic diffraction peaks of (100) and (002) as mentioned in the XRD results should be larger than that of CN. However, the actually measured BET surface area of Pt₁@CN (57.7 m² g⁻¹) was slightly smaller than that

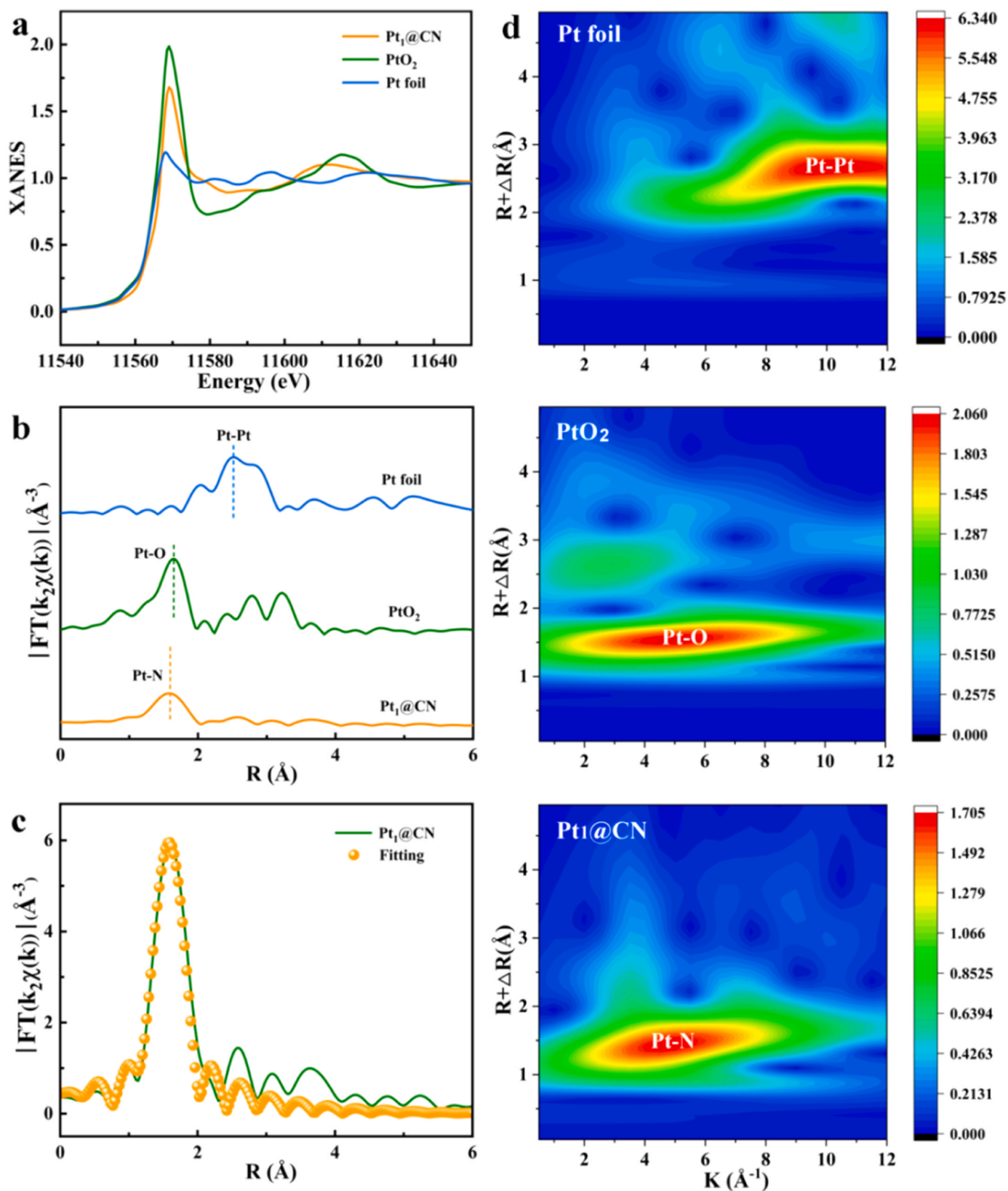


Fig. 2. (a) Pt L₃-edge XANES spectra and (b) k₂-weighted Fourier-transform EXAFS spectra for Pt₁@CN with Pt foil and PtO₂ as references, (c) the corresponding EXAFS R-space fitting curves of Pt₁@CN, (d) wavelet transforms of the k₂-weighted Pt L₃-edge EXAFS spectra of Pt foil, PtO₂, and Pt₁@CN.

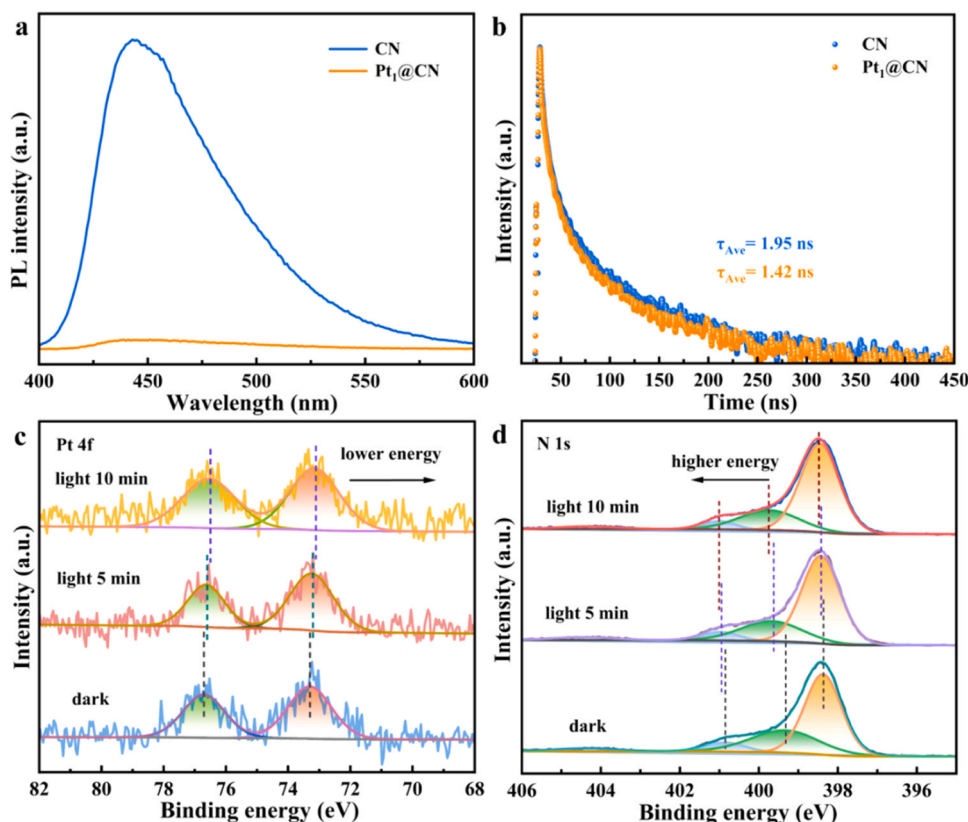


Fig. 3. (a) PL spectra and (b) TR-PL spectra of CN and Pt₁@CN, (c) XPS Pt-4f spectra, and (d) XPS N-1s spectra of Pt₁@CN in the dark and under light irradiation for 5 and 10 min.

of CN ($58.0 \text{ m}^2 \text{ g}^{-1}$), probably due to the unfavorable N₂ adsorption after the introduction of Pt single atoms [28,47,48]. The specific porous nanosheet morphology of Pt₁@CN would be beneficial for accommodating more Pt single atoms to serve as exposed active sites [49], expediting both the CO₂ molecule diffusion and charge transfer [50], strengthening incident light harvesting via multi-scattering and reflection during the catalytic reaction. Additionally, AC-HAADF-STEM and the corresponding elemental mapping images (Figs. 1b and 1c) indicated the uniform distribution of Pt, C, and N in the C₃N₄ support (refer to the isolated Pt atoms in yellow circles in Fig. 1b).

To investigate the chemical configuration and coordination environment of Pt₁@CN, X-ray absorption spectroscopy (XAS) and X-ray photoelectron spectroscopy (XPS) measurements were conducted. The peak intensity of X-ray absorption near-edge structure (XANES) of the 5d transition-metal L₃-edge is a good indicator for the number of unoccupied d-electron states [51]. The normalized Pt L₃-edge XANES spectra (Fig. 2a) showed that the white-line intensity for Pt₁@CN was higher than that for Pt foil but lower than that for PtO₂, indicating that the Pt single atoms in Pt₁@CN carried a partial positive charge ($\text{Pt}^{\delta+}$; $0 < \delta < 4$) [26,52–54]. This finding was consistent with the high-resolution Pt 4f XPS spectra, in which the peaks of Pt₁@CN shifted toward higher binding energies compared with those of metallic Pt that are usually located at 73.8 and 70.4 eV (Fig. S5) [55]. The results indicated the presence of a strong interaction between the Pt single atoms and the C₃N₄ support, which could be expected to facilitate the electron transport in catalytic reaction [56]. The k_2 -weighted Fourier-transformed extended X-ray absorption fine structure (EXAFS) spectra of Pt₁@CN showed a main peak at 1.51 \AA corresponding to the Pt–N coordination (Fig. 2b). Meanwhile, Pt–Pt (2.51 \AA) and Pt–O (1.63 \AA) bonds were not shown in Pt₁@CN, confirming the existence of Pt single atoms as evidenced by the AC-HAADF-STEM result (Fig. 1c). Using the optimally fitted EXAFS result of Pt₁@CN, the coordination number of N atoms in the first shell was estimated to be 3.7 at the distance of 1.97 \AA (Fig. 2c,

and the fitting parameters are shown in Table S1).

To elucidate the possible coordination between the Pt atoms and light elements (C/N/O) in Pt₁@CN more clearly, we carried out the wavelet transforms of the k_2 -weighted Pt L₃-edge EXAFS spectra for a high resolution in either k or R space [53,57]. As shown in Fig. 2d, the intensity maximum near 4.6 \AA^{-1} for Pt₁@CN could be assigned to the Pt–N coordination at $\sim 1.51 \text{ \AA}$ (R space); whereas, the maximum intensities at 10.3 and 5.3 \AA^{-1} corresponding to Pt–Pt coordination and Pt–O coordination in Pt foil and PtO₂, respectively, were not observed in Pt₁@CN. XPS spectra were also measured to further study the chemical states of Pt₁@CN. In the high-resolution XPS N 1s spectra of Pt₁@CN, the peaks ascribable to sp^2 -bonded N ($\text{C–N} = \text{C}$), sp^3 tertiary nitrogen N–C₃, and C–NH_x appeared at 398.4, 399.3, and 400.8 eV, respectively (Fig. S6). These peaks shifted toward higher binding energies in Pt₁@CN, indicating the electron transfer from N atoms to the anchored Pt single atoms [52,58]. In contrast, the high-resolution XPS C 1s spectra (Fig. S7) and O 1s spectra (Fig. S8) of Pt₁@CN and CN did not show an obvious difference, further suggesting that the unsaturated Pt single atoms were prone to coordinate with N atoms. In short, the EXAFS and XPS results demonstrated that the Pt single atoms were anchored on the CN framework by coordinating with four N atoms, being consistent with the theoretical Pt–N distance obtained from the optimized DFT structural model calculations (Fig. S9).

The UV–vis absorption spectra showed a red shift of the absorption edge and enhanced absorbance in the long wavelength range of Pt₁@CN compared to CN (Fig. S10a), which might be originated from the electron excitation from C₃N₄ to Pt atoms due to the strong affinity between C₃N₄ and Pt single atoms [25,28]. Moreover, the strong Pt–N₄ coordination might create extra states of $\text{Pt}^{\delta+}$, giving rise to enhanced absorbance of Pt₁@CN [59,60]. The electron excitation from the d band of metal atom to the conduction band of C₃N₄ [22] was not observed in the UV–vis absorption spectra of Pt₁@CN. According to the plots of $(ah\nu)^2$ versus photon energy ($h\nu$) in Fig. S10b, Pt₁@CN showed a narrower

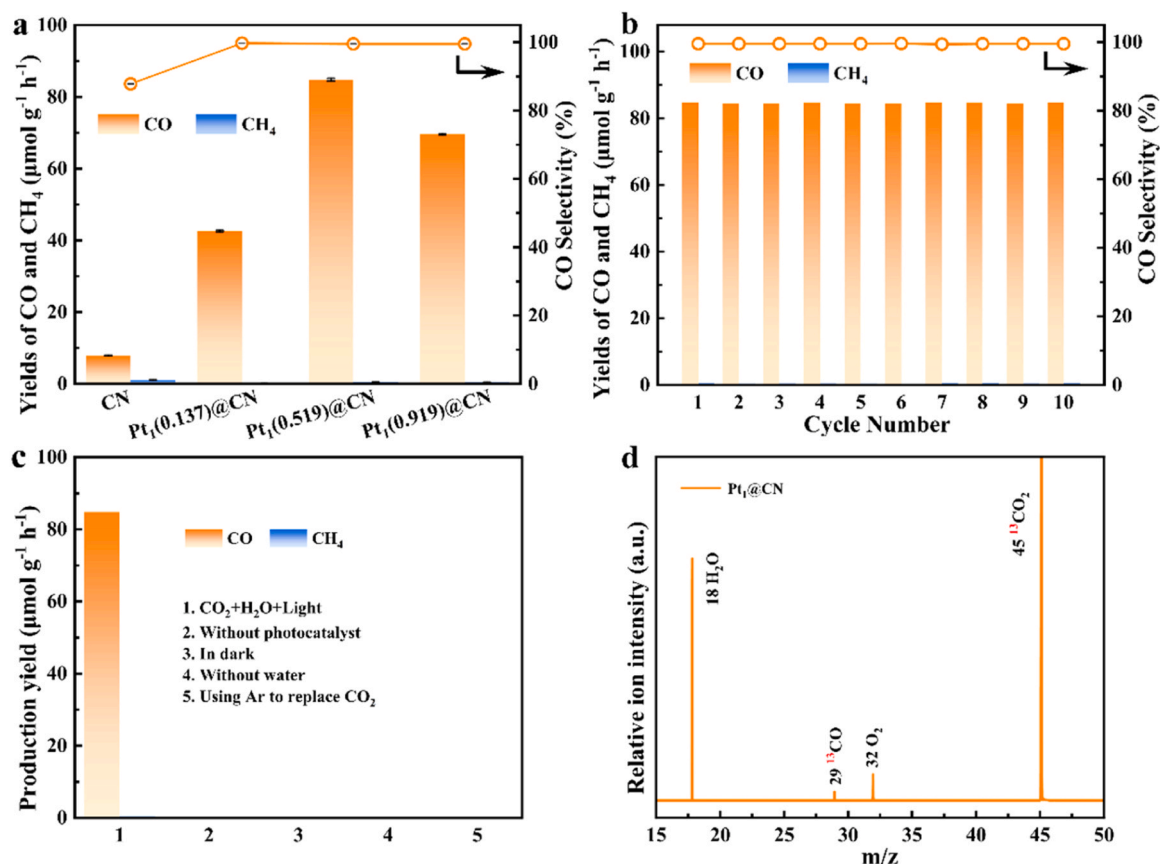


Fig. 4. (a) Yields of CO and CH₄ and CO selectivity over CN and Pt₁(x)@CN (x = 0.137, 0.519, 0.919 wt%), (b) stability test of CO₂ photoreduction over Pt₁@CN (the reaction time of each cycle was 1 h), (c) a series of blank experiments over Pt₁@CN, (d) SVUV-PIMS spectrum of the gas products after ¹³CO₂ photoreduction over Pt₁@CN at $h\nu = 14.3$ eV.

bandgap ($E_g = 2.59$ eV) than CN ($E_g = 2.69$ eV). Besides, the steady-state photoluminescence (PL) spectra and time-resolved photoluminescence (TR-PL) spectra were measured to probe the separation and transfer of photoinduced charge carriers [61]. The quenched PL intensity of Pt₁@CN revealed that the Pt single atoms promoted the separation and transfer of photoexcited charge carriers (Fig. 3a). Meanwhile, the TR-PL results indicated that the decay time decreased from 1.95 ns for CN to 1.42 ns for Pt₁@CN, further revealing that the Pt single atoms accelerated the transfer of electrons from C₃N₄ to the Pt active sites (Fig. 3b). The efficient separation and transfer of photoinduced charge carriers in Pt₁@CN could be attributed to the Pt–N₄ coordinated active sites on the C₃N₄ support. In addition, the electron paramagnetic resonance (EPR) spectrometry of Pt₁@CN under light irradiation showed a peak at the g value of 2.003, the intensity of which was higher than that of CN due to the enhanced density of photoexcited electrons by the introduction of Pt atoms in Pt₁@CN (Fig. S11) [62].

To verify the effective transfer of photogenerated electrons at the Pt–N₄ active sites, XPS measurements were used to investigate the distribution of the photogenerated electrons in the dark and under light irradiation. In the *quasi*-in-situ XPS Pt 4f spectra of Pt₁@CN (Fig. 3c), the two peaks of Pt shifted toward lower binding energies under light irradiation compared to those in dark, and the longer the irradiation time, the lower binding energy the peak shifted to. It indicated that the Pt single-atom sites on Pt₁@CN were prone to capturing the photogenerated electrons. On the contrary, all peaks of N 1s spectra shifted toward higher binding energies under light irradiation in comparison with those measured in dark (Fig. 3d). The above results clearly demonstrated that the Pt single atoms could effectively promote the separation and transfer of photogenerated electrons between C₃N₄ and Pt single atoms.

We investigated the CO₂ photoreduction performances over CN and Pt₁(x)@CN (x = 0.137, 0.519, 0.919 wt%) using H₂O as a reductant under irradiation with a 300 W Xe lamp and a standard AM 1.5 G filter. As can be seen in Fig. 4a, CN showed the evolution rates of 7.9 $\mu\text{mol g}^{-1} \text{h}^{-1}$ and 1.1 $\mu\text{mol g}^{-1} \text{h}^{-1}$ for CO and CH₄, respectively. Interestingly, the introduction of Pt single atoms dramatically improved the performance of Pt₁(x)@CN, especially the evolution rate and selectivity of CO while the CH₄ evolution was almost suppressed. With increasing the loaded Pt amount, the evolution rate of CO increased, and the best performance was obtained over Pt₁(0.519)@CN (abbreviated as Pt₁@CN) showing nearly 100% CO selectivity with an evolution rate of 84.8 $\mu\text{mol g}^{-1} \text{h}^{-1}$, which was ~10.7 times that of CN. The turnover frequency (TOF) of CO was 3.2 h^{−1} over Pt₁@CN (see details for calculation of TOF in Supplementary data). Further increasing the loaded Pt amount would decrease the intrinsic activity of Pt single atoms due to the shortened average inter-atom distance [63,64]. Besides, more Pt atoms would agglomerate or bury inside the inner part of C₃N₄ framework, resulting in reduced activity. The O₂ evolution rate over Pt₁@CN was determined to be 42.5 $\mu\text{mol g}^{-1} \text{h}^{-1}$, essentially in a balance with the CO₂ reduction to CO. The H₂ yield was poor, indicating that the competing HER was effectively suppressed since the theoretical calculations of free energies also revealed that in comparison with CN, the Pt–N₄ active sites in Pt₁@CN significantly increased *CO₂ adsorption while weakened *H adsorption (Fig. S12). Moreover, the apparent quantum efficiency (AQE) of 1.35% at 400 nm for CO evolution was achieved over Pt₁@CN. Under similar experimental conditions, our Pt₁@CN photocatalyst outperformed most previously reported C₃N₄-based single-atom photocatalysts in terms of CO evolution rate, selectivity, TOF and AQE values (Table S2). The excellent activity of Pt₁@CN with the unique Pt–N₄ coordination might be attributed to the good dispersion of Pt single atoms in the C₃N₄

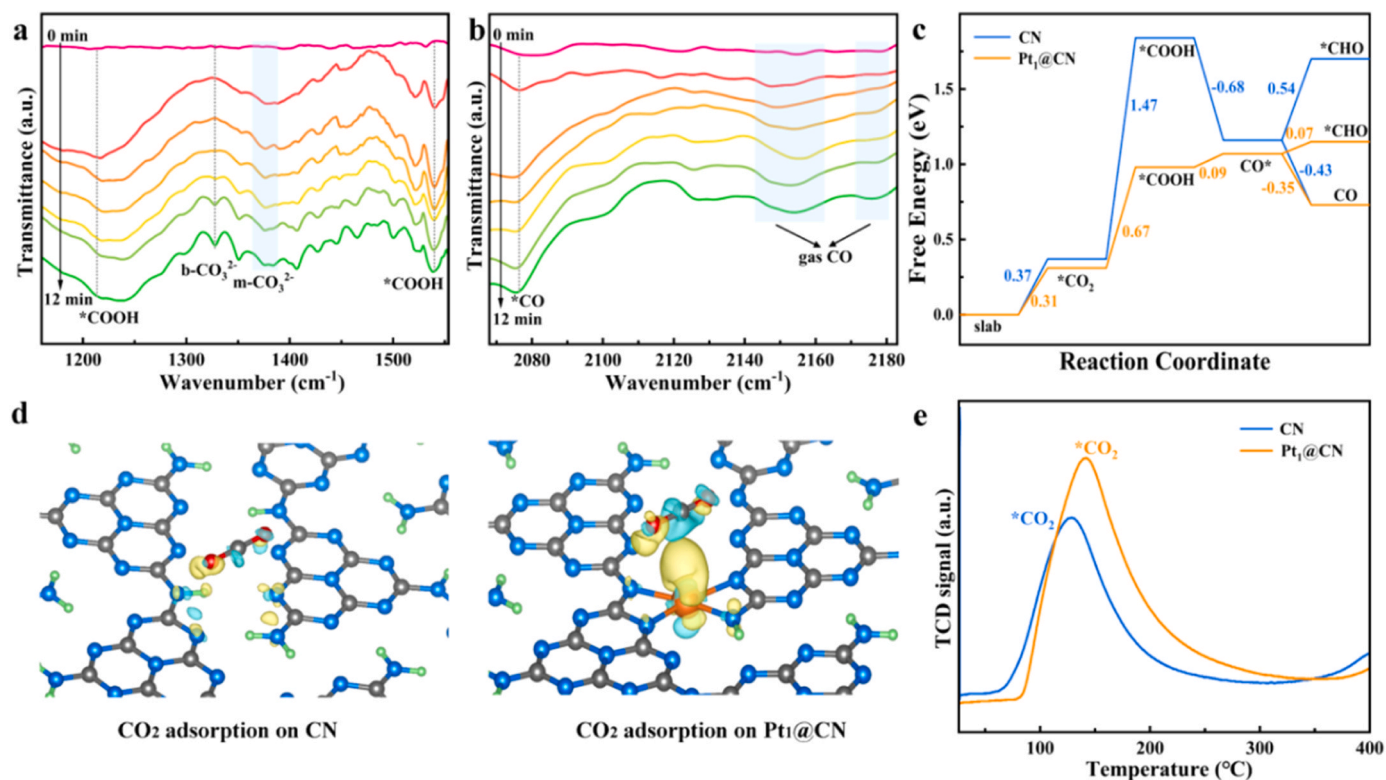


Fig. 5. (a, b) In situ DRIFT spectra of the CO₂ photoreduction process over Pt₁@CN using vaporized H₂O as a reductant. The curve marked with “0 min” was collected after 30 min of reaction with CO₂ and H₂O in the dark, (c) Gibbs free energies of CO₂ photoreduction pathways by DFT calculations for Pt₁@CN (Pt sites) and CN surfaces, (d) charge density differences after *CO₂ adsorption on CN and Pt₁@CN. Electron accumulation is in yellow, and electron depletion is in blue, (e) CO₂-TPD spectra of CN and Pt₁@CN.

framework, which provided more accessible active sites with appropriate inter-site distance of Pt atoms [63–66].

Additionally, Pt₁@CN showed no obvious decrease in the activity after ten consecutive cycles of CO₂ photoreduction, indicating its good photostability (Fig. 4b). Furthermore, the XRD pattern, FTIR and EXAFS spectra, and AC-HAADF-STEM images of Pt₁@CN demonstrated that the structures of Pt₁@CN and the Pt single atoms were well maintained after the photoreduction reaction, confirming the outstanding stability of Pt₁@CN (Fig. S13–S16). A series of blank experiments of Pt₁@CN were conducted to identify the reduction products, including reactions in the absence of CO₂, water, light irradiation, or photocatalyst. No CO or other carbon-based chemicals were detected (Fig. 4c). To unveil the origin of the reduction products, the ¹³CO₂-labeling experiment over Pt₁@CN was performed by the synchrotron-radiation vacuum ultraviolet photoionization mass spectrometry (SVUV-PIMS), which could effectively avoid the interference by the fragment ions in the process of photoionization [67,68]. The signal of ¹³CO (*m/z* = 29) confirmed that CO was solely originated from the photoreduction reaction of CO₂ with H₂O over Pt₁@CN, rather than through other substances or via the decomposition reaction of C₃N₄ (Fig. 4d) [69,70].

To investigate the intermediate products and acquire a deep understanding of the CO₂ photoreduction process over Pt₁@CN, in situ diffuse reflectance infrared Fourier transform (DRIFT) spectroscopy was performed for the photoreaction of CO₂ with H₂O over Pt₁@CN (see details in S1 of the Supporting Information). Under irradiation, the peaks corresponding to the *COOH group, the key intermediate in the CO₂ reduction to CO, appeared at 1210 and 1542 cm⁻¹ (Fig. 5a) [71]. The peak intensities of COOH* gradually increased with extending the irradiation time. Meanwhile, the characteristic infrared peaks of bidentate carbonate (b-CO₃²⁻, 1328 cm⁻¹) and monodentate carbonate (m-CO₃²⁻, 1382 cm⁻¹), which were derived from the CO₂ dissolved in H₂O, were detected [72]. As shown in Fig. 5b, the peaks of adsorbed

CO* (2076 cm⁻¹) and gas CO (2156 and 2178 cm⁻¹) were also observed, and the peak intensities gradually increased with the irradiation time, indicating the progress of CO gas production over Pt₁@CN. On the other hand, the blue-shift of the characteristic peak of gas CO might be due to the dipole-coupling between identical CO molecules [73,74]. Additionally, we performed the DFT calculations on the Gibbs free energies of CO₂ photoreduction reactions over Pt₁@CN and CN (see the adsorption configurations of related intermediates for Pt₁@CN and CN in Fig. S17). As shown in Fig. 5c, Pt₁@CN owned a much lower formation energy of COOH* (the rate-limiting step, 0.67 eV) than CN (1.47 eV), demonstrating that Pt₁@CN had a lower barrier of *CO₂-to-*COOH. Meanwhile, the nearly 100% CO selectivity might be attributed to the rapid dissociation of *CO groups on the Pt₁@CN surface to form CO molecules with smaller Gibbs free energy (–0.35 eV) than protonating of *CO to *CHO (0.07 eV). The above results suggest that Pt–N₄ coordinated active sites are advantageous for generating the *COOH intermediate, reducing the reaction barrier, lowering the activation energy of CO₂, and improving the CO₂ reduction activity and CO selectivity.

The interaction between the adsorbed CO₂ and the photocatalysts was studied by calculating the charge density. Notably, more electrons transferred to the adsorbed CO₂ molecules from Pt₁@CN than from CN (Fig. 5d). It indicated that the introduction of Pt–N₄ active sites would be beneficial for the adsorption and activation of CO₂, further promoting the CO₂ photoreduction activity. In addition, CO₂ temperature-programmed desorption (CO₂-TPD) spectroscopy was conducted to examine the adsorption–desorption behavior of CO₂ molecules. The peak between 50–350 °C could be assigned to the molecular adsorption of CO₂ appearing in the CO₂-TPD curves of Pt₁@CN and CN [75]. Clearly, Pt₁@CN showed stronger CO₂ adsorption and higher onset desorption temperature than CN, indicating that the Pt–N₄ coordinated active sites were favorable for CO₂ adsorption and activation (Fig. 5e).

CO temperature-programmed desorption (CO-TPD) spectra were also measured to examine the adsorption–desorption behavior of CO molecules. As displayed in Fig. S18, while there was no obvious difference between the CO desorption temperatures over CN and Pt₁@CN, the much less adsorption of CO on Pt₁@CN than on CN definitely indicated the favorable desorption of CO from the Pt₁@CN surface, which would increase the CO₂ photoreaction activity and CO selectivity.

Based on the above results and discussion, we propose the mechanism in Scheme 2 for the efficient CO₂ photoreduction activity and ~100% CO selectivity achieved over Pt₁@CN. The Pt–N₄ coordinated single atom active sites promote the separation/transfer of photo-generated charge carriers, facilitate the adsorption/activation of CO₂ molecules, formation of *COOH intermediate, desorption of *CO and evolution of CO, thereby accounting for the enhanced CO₂ photoreduction activity with ~100% CO selectivity. In short, the CO₂ photoreduction pathway over Pt₁@CN can be expressed as follows: CO₂ → *CO₂ → CO₃²⁻ → *COOH → *CO → CO↑.

4. Conclusions

In summary, we designed and synthesized Pt single atoms anchored on C₃N₄ nanosheets with a unique Pt–N₄ coordination. Compared with CN, the synthesized Pt₁@CN photocatalyst exhibited considerably enhanced CO₂ photoreduction activity and nearly 100% CO selectivity, outperforming most of the previously reported single-atom anchored C₃N₄-based photocatalysts for CO₂ photoreduction using H₂O as a reductant. Moreover, Pt₁@CN showed excellent long-term photocatalytic stability. Experimental and theoretical calculation results revealed that the Pt–N₄ coordinated single atoms served as the active sites to promote the dynamic transfer of photogenerated charge carriers, adsorption/activation of CO₂ molecules, generation of the *COOH intermediate, and desorption of *CO and evolution of CO, thus accounting for the enhanced CO₂ photoconversion with a high CO selectivity. This study suggests that constructing single-atom active sites in a suitable support is a feasible strategy for enhancing the CO₂ photoreduction efficiency and modulating the product selectivity.

CRediT authorship contribution statement

Shan Hu: Conceptualization, Data curation, Formal analysis, Investigation, Methodology, Writing – original draft. **Panzhe Qiao:** Data curation, Formal analysis, Investigation, Methodology, Resources. **Xinming Liang:** Data curation, Investigation. **Guiming Ba:** Data curation, Investigation. **Xiaolong Zu:** Formal analysis, Resources. **Huilin Hu:** Data curation, Investigation. **Jinhua Ye:** Funding acquisition, Supervision. **Defa Wang:** Conceptualization, Formal analysis, Funding acquisition, Supervision, Writing – review & editing.

Declaration of Competing Interest

The authors declare that they have no known competing financial interests or personal relationships that could have appeared to influence the work reported in this paper.

Data availability

Data will be made available on request.

Acknowledgements

This work was financially supported by the National Natural Science Foundation of China (51572191, 21633004). The authors thank the beamline BL14W1 (Shanghai Synchrotron Radiation Facility) for providing the beam time and the beamline BL20U (Shanghai Synchrotron Radiation Facility) for providing the TEM testing time.

Appendix A. Supporting information

Supplementary data associated with this article can be found in the online version at doi:10.1016/j.apcatb.2024.123737.

References

- [1] Y.O. Wang, E.Q. Chen, J.W. Tang, Insight on reaction pathways of photocatalytic CO₂ conversion, *ACS Catal.* 12 (2022) 7300–7316.
- [2] J. Gu, W. Chen, G.G. Shan, G. Li, C. Sun, X.L. Wang, Z. Su, The roles of polyoxometalates in photocatalytic reduction of carbon dioxide, *Mater. Today Energy* 21 (2021) 100760.
- [3] L.Z. Liu, S.B. Wang, H.W. Huang, Y.H. Zhang, T.Y. Ma, Surface sites engineering on semiconductors to boost photocatalytic CO₂ reduction, *Nano Energy* 75 (2020) 104959.
- [4] D. Pakhare, J. Spivey, A review of dry (CO₂) reforming of methane over noble metal catalysts, *Chem. Soc. Rev.* 43 (2014) 7813–7837.
- [5] J.Q. Lv, J.F. Xie, A.G.A. Mohamed, X. Zhang, Y.Y. Feng, J. Lei, E.B. Zhou, D. Q. Yuan, Y.B. Wang, Solar utilization beyond photosynthesis, *Nat. Rev. Chem.* 7 (2023) 91–105.
- [6] S.W. Gong, G.Q. Zhu, R. Wang, F. Rao, X.J. Shi, J.Z. Gao, Y. Huang, C.Z. He, M. Hojamberdiev, Synergistically boosting highly selective CO₂-to-CO photoreduction over BiOCl nanosheets via in-situ formation of surface defects and non-precious metal nanoparticles, *Appl. Catal. B Environ.* 297 (2021) 120413.
- [7] Y.J. Xiong, J.H. Ye, C. Zhao, Carbon dioxide conversion, *ChemNanoMat* 7 (2021) 967–968.
- [8] Z.F. Wang, Y. Hu, S.P. Zhang, Y. Sun, Artificial photosynthesis systems for solar energy conversion and storage: platforms and their realities, *Chem. Soc. Rev.* 51 (2022) 6704–6737.
- [9] H. Wang, H. Wang, Z.W. Wang, L. Tang, G.M. Zeng, P. Xu, M. Chen, T. Xiong, C. Y. Zhou, X.Y. Li, D.L. Huang, Y. Zhu, Z.X. Wang, J.W. Tang, Covalent organic framework photocatalysts: structures and applications, *Chem. Soc. Rev.* 49 (2020) 4135–4165.
- [10] Y. Wang, Z. Hu, W. Wang, Y.N. Li, H.C. He, L. Deng, Y. Zhang, J.H. Huang, N. Zhao, G.P. Yu, Y.N. Liu, Rational design of defect metal oxide/covalent organic frameworks Z-scheme heterojunction for photoreduction CO₂ to CO, *Appl. Catal. B Environ.* 327 (2023) 122419.
- [11] X. Li, J.G. Yu, M. Jaroniec, X.B. Chen, Cocatalysts for selective photoreduction of CO₂ into solar fuels, *Chem. Rev.* 119 (2019) 3962–4179.
- [12] S.F. Ji, Y.J. Chen, X.L. Wang, Z.D. Zhang, D.S. Wang, Y.D. Li, Chemical synthesis of single atomic site catalysts, *Chem. Rev.* 120 (2020) 11900–11955.
- [13] A.Q. Wang, J. Li, T. Zhang, Heterogeneous single-atom catalysis, *Nat. Rev. Chem.* 2 (2018) 65–81.
- [14] B.T. Qiao, A.Q. Wang, X.F. Yang, L.F. Allard, Z. Jiang, Y.T. Cui, J.Y. Liu, J. Li, T. Zhang, Single-atom catalysis of CO oxidation using Pt₁/FeO_x, *Nat. Chem.* 3 (2011) 634–641.
- [15] A.C.M. Loy, S.Y. Teng, B.S. How, X.X. Zhang, K.W. Cheah, V. Butera, W.D. Leong, B.L.F. Chin, C.L. Yiin, M.J. Taylor, G. Kyriakou, Elucidation of single atom catalysts for energy and sustainable chemical production: synthesis, characterization and frontier science, *Prog. Energy Combust. Sci.* 96 (2023) 101074.
- [16] J.F. Sun, Q.Q. Xu, J.L. Qi, D. Zhou, H.Y. Zhu, J.Z. Yin, Isolated single atoms anchored on N-doped carbon materials as a highly efficient catalyst for electrochemical and organic reactions, *ACS Sustain. Chem. Eng.* 8 (2020) 14630–14656.
- [17] P.G. Liu, Z.X. Huang, X.P. Gao, X. Hong, J.F. Zhu, G.M. Wang, Y.E. Wu, J. Zeng, X. S. Zheng, Synergy between palladium single atoms and nanoparticles via hydrogen spillover for enhancing CO₂ photoreduction to CH₄, *Adv. Mater.* 34 (2022) 2200057.
- [18] X.C. Wang, X.F. Chen, A. Thomas, X.Z. Fu, M. Antonietti, Metal-containing carbon nitride compounds: a new functional organic-metal hybrid material, *Adv. Mater.* 21 (2009) 1609–1612.
- [19] D. Liu, S.T. Chen, Y.X. Zhang, R.J. Li, T.Y. Peng, Modulating the bridging units of carbon nitride for highly efficient charge separation and visible-light-responsive photocatalytic H₂ evolution, *Appl. Catal. B Environ.* 333 (2023) 122805.
- [20] J.W. Fu, K. Liu, K.X. Jiang, H.J.W. Li, P.D. An, W.Z. Li, N. Zhang, H.M. Li, X.W. Xu, H.Q. Zhou, D.S. Tang, X.M. Wang, X.Q. Qiu, M. Liu, Graphitic carbon nitride with dopant induced charge localization for enhanced photoreduction of CO₂ to CH₄, *Adv. Sci.* 6 (2019) 1900796.
- [21] G.G. Zhang, G.S. Li, T. Heil, S. Zafeirotas, F.L. Lai, A. Savateev, M. Antonietti, X. C. Wang, Tailoring the grain boundary chemistry of polymeric carbon nitride for enhanced solar hydrogen production and CO₂ reduction, *Angew. Chem. Int. Ed.* 58 (2019) 3433–3437.
- [22] G.P. Gao, Y. Jiao, E.R. Wacławik, A.J. Du, Single atom (Pd/Pt) supported on graphitic carbon nitride as an efficient photocatalyst for visible-light reduction of carbon dioxide, *J. Am. Chem. Soc.* 138 (2016) 6292–6297.
- [23] X.L. Sui, L. Zhang, J.J. Li, K. Doyle-Davis, R.Y. Li, Z.B. Wang, X.L. Sun, Advanced support materials and interactions for atomically dispersed noble-metal catalysts: from support effects to design strategies, *Adv. Energy Mater.* 12 (2022) 2102556.
- [24] X.D. Xiao, Z.S.L. Ruan, Q. Li, L.P. Zhang, H.Y. Meng, Q. Zhang, H.L. Bao, B.J. Jiang, J. Zhou, C.Y. Guo, X.L. Wang, H.G. Fu, A unique Fe–N₄ coordination system enabling transformation of oxygen into superoxide for photocatalytic C–H activation with high efficiency and selectivity, *Adv. Mater.* 34 (2022) 2200612.

- [25] L.W. Zhang, R. Long, Y.M. Zhang, D.L. Duan, Y.J. Xiong, Y.J. Zhang, Y.P. Bi, Direct observation of dynamic bond evolution in single-atom Pt/C₃N₄, *Catal. Angew. Chem. Int. Ed.* 59 (2020) 6224–6229.
- [26] Y.D. Hu, Y.T. Qu, Y.S. Zhou, Z.Y. Wang, H.J. Wang, B. Yang, Z.Q. Yu, Y.E. Wu, Single Pt atom-anchored C₃N₄: a bridging Pt–N bond boosted electron transfer for highly efficient photocatalytic H₂ generation, *Chem. Eng. J.* 412 (2021) 128749.
- [27] P. Chen, B. Lei, X.A. Dong, H. Wang, J.P. Sheng, W. Cui, J.Y. Li, Y.J. Sun, Z. M. Wang, F. Dong, Rare-earth single-atom La–N charge-transfer bridge on carbon nitride for highly efficient and selective photocatalytic CO₂ reduction, *ACS Nano* 14 (2020) 15841–15852.
- [28] S. Hu, P.Z. Qiao, X.L. Yi, Y.M. Lei, H.L. Hu, J.H. Ye, D.F. Wang, Selective photocatalytic reduction of CO₂ to CO mediated by silver single atoms anchored on tubular carbon nitride, *Angew. Chem. Int. Ed.* 62 (2023) e202304585.
- [29] Y.M. Cai, J.J. Fu, Y. Zhou, Y.C. Chang, Q.H. Min, J.J. Zhu, Y.H. Lin, W.L. Zhu, Insights on forming N,O-coordinated Cu single-atom catalysts for electrochemical reduction CO₂ to methane, *Nat. Commun.* 12 (2021) 586.
- [30] X. Liang, N.H. Fu, S.C. Yao, Z. Li, Y.D. Li, The progress and outlook of metal single-atom-site catalysis, *J. Am. Chem. Soc.* 144 (2022) 18155–18174.
- [31] R. Arrigo, M.E. Schuster, Z.L. Xie, Y.M. Yi, G. Wosnick, L.L. Sun, K.E. Hermann, M. Friedrich, P. Kast, M. Hävecker, A. Knop-Gericke, R. Schlögl, Nature of the N–Pd interaction in nitrogen-doped carbon nanotube catalysts, *ACS Catal.* 5 (2015) 2740–2753.
- [32] S.J. Liang, X.H. Zhong, Z.Q. Zhong, H. Deng, W.Y. Wong, Highly dispersed nickel site catalysts for diluted CO₂ photoreduction to CO with nearly 100% selectivity, *Appl. Catal. B Environ.* 337 (2023) 122958.
- [33] C.Y. Dong, C. Lian, S.C. Hu, Z.S. Deng, J.Q. Gong, M.D. Li, H.L. Liu, M.Y. Xing, J. L. Zhang, Size-dependent activity and selectivity of carbon dioxide photocatalytic reduction over platinum nanoparticles, *Nat. Commun.* 9 (2018) 1252.
- [34] N. Denisov, S.S. Qin, J. Will, B.N. Vasiljevic, N.V. Skorodumova, I.A. Pašti, B. B. Sarma, B. Osuagwu, T. Yokosawa, J. Voss, J. Wirth, E. Spiecker, P. Schmuk, Light-induced agglomeration of single-atom platinum in photocatalysis, *Adv. Mater.* 35 (2023) 2206569.
- [35] W.N. Wang, W.J. An, B. Ramalingam, S. Mukherjee, D.M. Niedzwiedzki, S. Gangopadhyay, P. Biswas, Size and structure matter: enhanced CO₂ photoreduction efficiency by size-resolved ultrafine Pt nanoparticles on TiO₂ single crystals, *J. Am. Chem. Soc.* 134 (2012) 11276–11281.
- [36] G. Kresse, J. Hafner, Ab initio molecular dynamics for liquid metals, *Phys. Rev. B* 47 (1993) 558–561.
- [37] G. Kresse, J. Furthmüller, Efficient iterative schemes for ab initio total-energy calculations using a plane-wave basis set, *Phys. Rev. B* 54 (1996) 11169–11186.
- [38] J.P. Perdew, K. Burke, M. Ernzerhof, Generalized gradient approximation made simple, *Phys. Rev. Lett.* 77 (1996) 3865–3868.
- [39] P.E. Blöchl, Projector augmented-wave method, *Phys. Rev. B* 50 (1994) 17953–17979.
- [40] S. Grimme, J. Antony, S. Ehrlich, H. Krieg, A consistent and accurate ab initio parametrization of density functional dispersion correction (DFT-D) for the 94 elements H–Pu, *J. Chem. Phys.* 132 (2010) 154104.
- [41] J.K. Nørskov, J. Rossmeisl, A. Logadottir, L. Lindqvist, J.R. Kitchin, T. Bligaard, H. Jónsson, Origin of the overpotential for oxygen reduction at a fuel-cell cathode, *J. Phys. Chem. B* 108 (2004) 17886–17892.
- [42] K. Mathew, R. Sundaraman, K. Letchworth-Weaver, T.A. Arias, R.G. Hennig, Implicit solvation model for density-functional study of nanocrystal surfaces and reaction pathways, *J. Chem. Phys.* 140 (2014) 084106.
- [43] J. Paier, R. Hirschi, M. Marsman, G. Kresse, The Perdew–Burke–Ernzerhof of exchange–correlation functional applied to the G2-1 test set using a plane-wave basis set, *J. Chem. Phys.* 122 (2005) 234102.
- [44] E.H. Zhang, L. Tao, J.K. An, J.W. Zhang, L.Z. Meng, X.B. Zheng, Y. Wang, N. Li, S. X. Du, J.T. Zhang, D.S. Wang, Y.D. Li, Engineering the local atomic environments of indium single-atom catalysts for efficient electrochemical production of hydrogen peroxide, *Angew. Chem. Int. Ed.* 61 (2022) e202117347.
- [45] Y. Chen, R.J. Guo, X.Y. Peng, X.Q. Wang, X.J. Liu, J.Q. Ren, J. He, L.C. Zhuo, J. Q. Sun, Y.F. Liu, Y.E. Wu, J. Luo, Highly productive electrosynthesis of ammonia by ad-molecule-targeting single Ag sites, *ACS Nano* 14 (2020) 6938–6946.
- [46] T. Yang, X.N. Mao, Y. Zhang, X.P. Wu, L. Wang, M.Y. Chu, C.W. Pao, S.Z. Yang, Y. Xu, X.Q. Huang, Coordination tailoring of Cu single sites on C₃N₄ realizes selective CO₂ hydrogenation at low temperature, *Nat. Commun.* 12 (2021) 6022.
- [47] P.Y. Dong, Y. Wang, A.C.J. Zhang, T. Cheng, X.G. Xi, J.L. Zhang, Platinum single atoms anchored on a covalent organic framework: boosting active sites for photocatalytic hydrogen evolution, *ACS Catal.* 11 (2021) 13266–13279.
- [48] S. Hoang, Y.B. Guo, A.J. Binder, W.X. Tang, S.B. Wang, J.Y. Liu, H. Tran, X.X. Lu, Y. Wang, Y. Ding, E.A. Kyriakidou, J. Yang, T.J. Toops, T.R. Pauly, R. Ramprasad, P.X. Gao, Activating low-temperature diesel oxidation by single-atom Pt on TiO₂ nanowire array, *Nat. Commun.* 11 (2020) 1062.
- [49] F. Chen, X.L. Wu, C.Y. Shi, H.J. Lin, J.R. Chen, Y.P. Shi, S.B. Wang, X.G. Duan, Molecular engineering toward pyrrolic N-rich M–N₄ (M = Cr, Mn, Fe, Co, Cu) single-atom sites for enhanced heterogeneous fenton-like reaction, *Adv. Funct. Mater.* 31 (2021) 2007877.
- [50] A. Thomas, A. Fischer, F. Goettmann, M. Antonietti, J.O. Müller, R. Schlögl, J. M. Carlsson, Graphitic carbon nitride materials: variation of structure and morphology and their use as metal-free catalysts, *J. Mater. Chem.* 18 (2008) 4893–4908.
- [51] J.F. Sui, H. Liu, S.J. Hu, K. Sun, G. Wan, H. Zhou, X. Zheng, H.L. Jiang, A general strategy to immobilize single-atom catalysts in metal–organic frameworks for enhanced photocatalysis, *Adv. Mater.* 34 (2022) 2109203.
- [52] Z.Q. Zhang, Y.G. Chen, L.Q. Zhou, C. Chen, Z. Han, B.S. Zhang, Q. Wu, L.J. Yang, L. Y. Du, Y.F. Bu, P. Wang, X.Z. Wang, H. Yang, Z. Hu, The simplest construction of single-site catalysts by the synergism of micropore trapping and nitrogen anchoring, *Nat. Commun.* 10 (2019) 1657.
- [53] Y.J. Chen, S.F. Ji, Y.G. Wang, J.C. Dong, W.X. Chen, Z. Li, R. Shen, L.R. Zheng, Z. B. Zhuang, D.S. Wang, Y.D. Li, Isolated single iron atoms anchored on N-doped porous carbon as an efficient electrocatalyst for the oxygen reduction reaction, *Angew. Chem. Int. Ed.* 56 (2017) 6937–6941.
- [54] X.J. Shi, Y. Huang, Y.N. Bo, D.L. Duan, Z.Y. Wang, J.J. Cao, G.Q. Zhu, W. Ho, L. Q. Wang, T.T. Huang, Y.J. Xiong, Highly selective photocatalytic CO₂ methanation with water vapor on single-atom platinum-decorated defective carbon nitride, *Angew. Chem. Int. Ed.* 61 (2022) e202203063.
- [55] A. Li, Q. Cao, G.Y. Zhou, B.V.K.J. Schmidt, W.J. Zhu, X.T. Yuan, H.L. Huo, J. L. Gong, M. Antonietti, Three-phase photocatalysis for the enhanced selectivity and activity of CO₂ reduction on a hydrophobic surface, *Angew. Chem. Int. Ed.* 58 (2019) 14549–14555.
- [56] C. Li, Z. Chen, H. Yi, Y. Cao, L. Du, Y.D. Hu, F.P. Kong, R.K. Campen, Y.Z. Gao, C. Y. Du, G.P. Yin, L.Y. Zhang, Y.J. Tong, Polyvinylpyrrolidone-coordinated single-site platinum catalyst exhibits high activity for hydrogen evolution reaction, *Angew. Chem. Int. Ed.* 59 (2020) 15902–15907.
- [57] H.L. Fei, J.C. Dong, M.J. Arellano-Jiménez, G.L. Ye, N.D. Kim, E.L.G. Samuel, Z. W. Peng, Z. Zhu, F. Qin, J.M. Bao, M.J. Yacaman, P.M. Ajayan, D.L. Chen, J. M. Tour, Atomic cobalt on nitrogen-doped graphene for hydrogen generation, *Nat. Commun.* 6 (2015) 8668.
- [58] X.W. Shi, C. Dai, X. Wang, J.Y. Hu, J.Y. Zhang, L.X. Zheng, L. Mao, H.J. Zheng, M. S. Zhu, Protruding Pt single-sites on hexagonal ZnIn₂S₄ to accelerate photocatalytic hydrogen evolution, *Nat. Commun.* 13 (2022) 1287.
- [59] L. Cheng, H. Yin, C. Cai, J.J. Fan, Q.J. Xiang, Single Ni atoms anchored on porous few-layer g-C₃N₄ for photocatalytic CO₂ reduction: the role of edge confinement, *Small* 16 (2020) 2002111.
- [60] Y.R. Li, Z.W. Wang, T. Xia, H.X. Ju, K. Zhang, R. Long, Q. Xu, C.M. Wang, L. Song, J.F. Zhu, J. Jiang, Y.J. Xiong, Implementing metal-to-ligand charge transfer in organic semiconductor for improved visible-near-infrared photocatalysis, *Adv. Mater.* 28 (2016) 6959–6965.
- [61] S. Hu, P.Z. Qiao, L.P. Zhang, B.J. Jiang, Y.T. Gao, F. Hou, B.G. Wu, Q. Li, Y. Jiang, C.G. Tian, W. Zhou, G.H. Tian, H.G. Fu, Assembly of TiO₂ ultrathin nanosheets with surface lattice distortion for solar-light-driven photocatalytic hydrogen evolution, *Appl. Catal. B Environ.* 239 (2018) 317–323.
- [62] Q. Liu, T.X. Chen, Y.R. Guo, Z.G. Zhang, X.M. Fang, Ultrathin g-C₃N₄ nanosheets coupled with carbon nanodots as 2D/0D composites for efficient photocatalytic H₂ evolution, *Appl. Catal. B Environ.* 193 (2016) 248–258.
- [63] Y.J. Ren, Y. Tang, L.L. Zhang, X.Y. Liu, L. Li, S. Miao, S.D. Su, A.Q. Wang, J. Li, T. Zhang, Unraveling the coordination structure–performance relationship in Pt₁/Fe₂O₃ single-atom catalyst, *Nat. Commun.* 10 (2019) 4500.
- [64] T.Y. Jing, T.T. Li, D.W. Rao, M.Y. Wang, Y.P. Zuo, Defining the loading of single-atom catalysts: weight fraction or atomic fraction? *Mater. Today Energy* 31 (2023) 101197.
- [65] A. Mehmood, M.J. Gong, F. Jaouen, A. Roy, A. Zitolo, A. Khan, M.T. Sougrati, M. Primbs, A.M. Bonastre, D. Fongalland, G. Drazic, P. Strasser, A. Kucernak, High loading of single atomic iron sites in Fe–NC oxygen reduction catalysts for proton exchange membrane fuel cells, *Nat. Catal.* 5 (2022) 311–323.
- [66] M. Primbs, Y.Y. Sun, A. Roy, D. Malko, A. Mehmood, M.T. Sougrati, P. Y. Blanchard, G. Granozzi, T. Kosmala, G. Daniel, P. Atanassov, J. Sharman, C. Durante, A. Kucernak, D. Jones, F. Jaouen, P. Strasser, Establishing reactivity descriptors for platinum group metal (PGM)-free Fe–N–C catalysts for PEM fuel cells, *Energy Environ. Sci.* 13 (2020) 2480–2500.
- [67] S.Y. Wang, B. Jiang, J. Henzie, F.Y. Xu, C.Y. Liu, X.G. Meng, S.R. Zou, H. Song, Y. Pan, H.X. Li, J.G. Yu, H. Chen, J.H. Ye, Designing reliable and accurate isotope-tracer experiments for CO₂ photoreduction, *Nat. Commun.* 14 (2023) 2534.
- [68] J.Q. Xu, Z.Y. Ju, W. Zhang, Y. Pan, J.F. Zhu, J.W. Mao, X.L. Zheng, H.Y. Fu, M. L. Yuan, H. Chen, R.X. Li, Efficient infrared-light-driven CO₂ reduction over ultrathin metallic Ni-doped CoS₂ nanosheets, *Angew. Chem. Int. Ed.* 60 (2021) 8705–8709.
- [69] X.L. Zu, Y. Zhao, X.D. Li, R.H. Chen, W.W. Shao, L. Li, P.Z. Qiao, W.S. Yan, Y. Pan, Q. Xu, J.F. Zhu, Y.F. Sun, Y. Xie, Reversible switching Cu^{II}/Cu^I single sites catalyze high-rate and selective CO₂ photoreduction, *Angew. Chem. Int. Ed.* 62 (2022) e202215247.
- [70] P. Chen, X.A. Dong, M. Huang, K.L. Li, L. Xiao, J.P. Sheng, S. Chen, Y. Zhou, F. Dong, Rapid self-decomposition of g-C₃N₄ during gas–solid photocatalytic CO₂ reduction and its effects on performance assessment, *ACS Catal.* 12 (2022) 4560–4570.
- [71] X.C. Jiao, Z.W. Chen, X.D. Li, Y.F. Sun, S. Gao, W.S. Yan, C.M. Wang, Q. Zhang, Y. Lin, Y. Luo, Y. Xie, Defect-mediated electron–hole separation in one-unit-cell ZnIn₂S₄ layers for boosted solar-driven CO₂ reduction, *J. Am. Chem. Soc.* 139 (2017) 7586–7594.
- [72] L. Cheng, X.Y. Yue, L.X. Wang, D.N. Zhang, P. Zhang, J.J. Fan, Q.J. Xiang, Dual-single-atom tailoring with bifunctional integration for high-performance CO₂ photoreduction, *Adv. Mater.* 33 (2021) 2105135.
- [73] A.S. Malkani, J. Li, N.J. Oliveira, M. He, X. Chang, B. Xu, Q. Lu, Understanding the electric and nonelectric field components of the cation effect on the electrochemical CO reduction reaction, *Sci. Adv.* 6 (2020) eabd2569.
- [74] C.M. Gunathunge, J.Y. Li, X. Li, M.M. Waegle, Surface-adsorbed CO as an infrared probe of electrocatalytic interfaces, *ACS Catal.* 10 (2020) 11700–11711.
- [75] L. Ran, Z.W. Li, B. Ran, J.Q. Cao, Y. Zhao, T. Shao, Y.R. Song, M.K.H. Leung, L. C. Sun, J.G. Hou, Engineering single-atom active sites on covalent organic frameworks for boosting CO₂ photoreduction, *J. Am. Chem. Soc.* 37 (2022) 17097–17109.